**Atmospheric
Measurement
Techniques**

Time dependent profile retrieval of UV/vis absorbing radicals from balloon-borne limb measurements – a case study on NO_2 and O_3

L. Kritten[1], A. Butz[2], M. Dorf[1], T. Deutschmann[1], S. Kühl[3], C. Prados-Roman[1], J. Pukīte[3], A. Rozanov[4], R. Schofield[5], and K. Pfeilsticker[1]

[1]Institute of Environmental Physics (IUP), University of Heidelberg, Heidelberg, Germany
[2]SRON – Netherlands Institute for Space Research, Utrecht, The Netherlands
[3]Max Planck Institute for Chemistry, Mainz, Germany
[4]Institute of Environmental Physics (IUP), University of Bremen, Bremen, Germany
[5]Alfred Wegener Institute for Polar and Marine Research (AWI), Potsdam, Germany

Abstract. A new "Bayesian" minimization algorithm for the retrieval of the diurnal variation of UV/vis absorbing radicals (O_3, NO_2, BrO, OClO and HONO) from balloon-borne limb scattered skylight observations is discussed. The method evaluates spectroscopic measurements in combination with radiative transfer calculations to drive a mathematical inversion on a discrete time and height grid. Here, the proposed method is applied to data obtained during two deployments of the mini-DOAS instrument on different balloon payloads in northern Brazil in June 2005. The retrieval is tested by comparing the inferred profiles to in-situ ozone sounding data and to measurements of the ENVISAT/SCIAMACHY satellite instrument performed during a collocated overpass. The comparison demonstrates the strength and validity of our approach. In particular for time-varying radical concentrations, photochemical corrections due to temporal mismatch of the corresponding observations are rendered dispensable. Thus, limb scanning UV/vis spectrometry from balloon platforms offers a more direct and concise approach for satellite validation of radical measurements than solar occultation measurements. Furthermore, monitoring of the diurnal variation of stratospheric radicals allows us to constrain photochemical parameters which are critical for stratospheric ozone chemistry, such as the photolysis frequency of N_2O_5 by observations of the diurnal variation of NO_2.

Correspondence to: L. Kritten
(lkritten@iup.uni-heidelberg.de)

1 Introduction

In the past decade balloon-borne remote sensing evolved into a powerful tool for the investigation of atmospheric parameters and photochemical processes relevant for stratospheric ozone chemistry. These spectroscopic techniques have been developed to remotely detect a wide range of stratospheric trace gases via their spectral signatures. Today, such techniques virtually cover all wavelengths ranging from the UV/visible over the near-IR and mid-IR into the microwave. Accordingly, a variety of instruments have been designed to passively monitor the atmospheric emission in the IR and microwave or the atmospheric absorption in the UV/vis and shortwave IR solar spectra (e.g. Pommereau and Goutail, 1988; Oelhaf et al., 1991; Toon et al., 1991; Camy-Peyret, 1995; Ferlemann et al., 2000; Birk et al., 2004). In particular, observations in the UV/vis spectral range facilitate monitoring of several important species such as O_3, NO_2, NO_3, HONO, BrO, IO, OIO, OClO, CH_2O and CH_2O_2. Balloon-borne solar occultation measurements have proven to be a particularly valuable tool for investigating stratospheric photochemistry (Ferlemann et al., 2000) and trends in stratospheric species, such as total bromine (Dorf et al., 2006). Here, we report on an extension of our previous studies on balloon-borne UV/vis scattered skylight limb observations (Weidner et al., 2005). While in previous studies we mainly considered measurements at fixed elevation angles during balloon ascent, here the limb method is expanded to observations from balloon float altitude at varying elevation

angles. They support the monitoring of stratospheric radicals at changing illumination.

In the past years such measurements were performed by our group from various azimuth angle controlled balloon gondolas, such as LPMA/DOAS (Laboratoire de Physique Moléculaire pour l'Atmosphère et l'Astrophysique and Differential Optical Absorption Spectroscopy), LPMA-IASI (Infrared Atmospheric Sounding Interferometer) and MIPAS-B (Michelson Interferometer for Passive Atmospheric Sounding-Balloon). Among a larger series of stratospheric balloon flights (see Table 1), favorable conditions for long duration observations, which are necessary to study the diurnal variation of radicals, were only met a limited number of times. Those flights were performed from the tropical station Teresina, Brazil (5.1° S, 42.9° W) in 2005 and 2008, or in high-latitude summer 2002 (Kiruna, Sweden, 67.9° N, 22.1° E) during turn-over of the stratospheric circulation. Typically, these balloon flights lasted in excess of 5 h at daytime.

While the present study mainly discusses details of the method to infer the diurnal variation of radical profiles, forthcoming studies will address the interpretation of the results with respect to stratospheric photochemistry. Section 2 introduces the applied methods with focus on instrument performance and spectral retrieval, followed by a description of the concentration profile retrieval including radiative transfer modelling and inversion through an optimal estimation method (Rodgers, 2000). Further, the profile retrieval is characterized by means of resolution in altitude and time. The information content and errors due to noise or unstable pointing are estimated. Section 3 reports on the validation of our approach for gases of (a) small diurnal variation such as O_3 and (b) large diurnal variation such as NO_2, by comparing our trace gas retrievals to (a) an O_3 profile measured by an ozone sonde, and (b) NO_2 profiles measured by the SCIA-MACHY instrument abord the ENVISAT satellite during a colocated overpass. Concluding remarks are given in Sect. 4.

2 Method

Radical profiling by UV/vis limb scattered skylight observations involves a couple of tools and methods. These rely on detailed knowledge of the measurement process (Sect. 2.1), dedicated methods for spectral (Sect. 2.2) and profile retrieval (Sect. 2.3) and thorough characterization of various sources of error (Sect. 2.4).

2.1 Instrument and measurements

A detailed description of the instrument is given by Weidner et al. (2005). Therefore, only a brief summary of instrumental details is given here. The mini-DOAS instrument is of light weight (7 kg) and low power consumption (10 W), and thus, can easily be deployed on remote sensing balloon

payloads or aircrafts. In its core the instrument houses two temperature and pressure stabilized commercial Ocean Optics spectrometers (USB/2000 (f/4)) covering the wavelength range from 340 to 500 nm at a spectral resolution of 0.8-1 nm (USB/2000) with 8 to 10 detector pixels/Full width at Half Maximum (FWHM) of the instrument response function, depending on wavelength. The telescope collimates scattered light into a glass fiber bundle with a vertical field of view (FOV) of 0.2°, thus allowing for a reasonably high altitude resolution. The measurement geometry is characterized by the elevation angle of the telescope (EA), the relative azimuth angle between telescope and the sun (SRAA) and the solar zenith angle (SZA). Routinely, the telescope is oriented to the horizon at a fixed EA during balloon ascent when the gondola ascends through the atmosphere, providing a large sensitivity for trace gases at the particular tangent height. A second mode of operation, which is the focus of the present paper, starts when the balloon has reached float altitude (e.g. around 35 km, see Fig. 1). Then the telescope is commanded to automatically scan different elevations ranging from EA = 0° to EA = −6° in steps of 0.5°. A full scan typically takes 15 min. The change in observation geometry leads to a changing sensitivity in different altitudes of the atmosphere, e.g. with the highest sensitivity at flight altitude (for EA ≈ 0°) or 20 km below (for EA ≈ −6°). Hence, by continuously scanning the atmosphere, the instrument provides time-resolved vertical profile information of UV/vis absorbing trace gases. Depending on the balloon payload, the float duration varies between several hours up to a whole day.

In order to retrieve profiles of the targeted trace gases from the measured spectral intensities, a two step approach is used. First, we infer the integrated concentration along the light path relative to a background integrated concentration from the measured spectra. In the following these are called differential slant column densities (∆SCDs). The applied method is the well-known DOAS technique (Platt and Stutz, 2008). In a second step, the inferred ∆SCDs are taken as input for a profile inversion algorithm that exploits the geometry of the light path aiming at the retrieval of vertical concentration profiles at different times.

2.2 Spectral retrieval

Following the approach described in Weidner et al. (2005), the measured spectra are analyzed for UV/vis absorbers (see Introduction) using the conventional DOAS method (Platt and Stutz, 2008). The ∆SCDs are derived by a non-linear least squares fit of measured intensities $I_i(\lambda)$ to a background intensity (henceforth $I_{ref}(\lambda)$) where the subscript i labels the i-th measurement and λ explicitly indicates that the measured intensities are wavelength dependent. Forward parameters are the (differential) absorption cross sections for individual absorbers and a Ring spectrum (Grainger and Ring, 1962). In addition atmospheric broad band extinction and
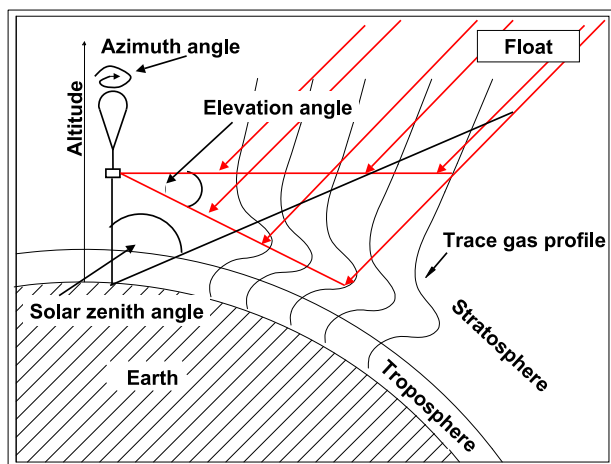
Fig. 1. Observation geometry of balloon-borne limb scattered sky-light measurements.

spectrometer stray light are respectively expressed as a multiplicative and additive polynomials, of which the coefficients are retrieved by the least squares fit (Fayt and Van Roozendael, 2001).

Considering for simplicity only a single molecular absorber with absorption cross section σ, Beer-Lambert's law of absorption is given by

$$I_i = I_0 \cdot \exp(-\sigma \cdot \mathrm{SCD}_i), \tag{1}$$

where SCD_i is the absorber slant column density with respect to a top-of-the-atmosphere solar spectrum I_0 that contains no absorption by the target species (the dependency on wavelength λ is from now on implicitly assumed). Note that since the extraterrestrial solar spectrum I_0 is not accessible to balloon-borne spectroscopy, all measurements are taken relative to a (Fraunhofer) background I_{ref}, which contains a residual atmospheric absorption $\mathrm{SCD}_{\mathrm{ref}}$. By a proper of I_{ref} $\mathrm{SCD}_{\mathrm{ref}}$ is minimized. Beer-Lambert's law for I_{ref} reads

$$I_{\mathrm{ref}} = I_0 \cdot \exp(-\sigma \cdot \mathrm{SCD}_{\mathrm{ref}}), \tag{2}$$

which is equivalent to

$$I_0 = I_{\mathrm{ref}} \cdot \exp(\sigma \cdot \mathrm{SCD}_{\mathrm{ref}}). \tag{3}$$

Inserting Eq. (3) into (1) leads to

$$\begin{aligned} I_i &= I_{\mathrm{ref}} \cdot \exp(\sigma \cdot \mathrm{SCD}_{\mathrm{ref}}) \exp(-\sigma \cdot \mathrm{SCD}_i) \\ &= I_{\mathrm{ref}} \cdot \exp(-\sigma \cdot [\mathrm{SCD}_i - \mathrm{SCD}_{\mathrm{ref}}]) \\ &= I_{\mathrm{ref}} \cdot \exp(-\sigma \cdot \Delta\mathrm{SCD}_i). \end{aligned} \tag{4}$$

The DOAS retrieval fits Eq. (4) to the measured intensity minimizing the least squares criterion by adjusting $\Delta\mathrm{SCD}_i$ and auxiliary parameters as described above. Hence, the result of a DOAS retrieval is a set of $\Delta\mathrm{SCD}_i$ ($i = 1, \dots, N$, with N the number of measurements). It is noteworthy that, in

principle, any measured spectrum I_i can serve as the reference spectrum I_{ref}. It is not necessary that the absorption or SCD is zero, as shown before in Eqs. (2) to (4). The choice of I_{ref} translates into a common offset for all $\Delta\mathrm{SCD}_i$ ($i = 1, \dots, N$), which in particular implies that a negative $\Delta\mathrm{SCD}_i$ is physically reasonable. Practically, a spectral analysis is performed using an arbitrary spectrum as I_{ref} in order to define a spectrum with low absorption, which is then chosen as final I_{ref} in order to increase the relative absorption and therefore decrease the relative error. Accordingly this choice may differ for different absorbers.

Here, we focus on test cases for gases such as O_3 and NO_2 that show small and large diurnal variations, respectively, and that can be validated through other measurement techniques. The spectral retrieval of O_3 and NO_2 is implemented as follows. The non-linear spectral fit is performed using the WinDOAS software (Fayt and Van Roozendael, 2001). It considers O_3 cross-sections for temperatures $T = 223\,\mathrm{K}$ and $203\,\mathrm{K}$ (orthogonalized to the former) taken from Voigt et al. (2001), both corrected for the I_0-Effect (Aliwell et al., 2002), an O_4 cross-section (at room temperature) from Hermans (2002), NO_2 cross-sections at temperatures $T = 230\,\mathrm{K}$ and $T = 217\,\mathrm{K}$ (orthogonalized to the former) from Harder et al. (1997), and an H_2O cross-section from Rothman et al. (2005). A 4th order polynomial is used to account for the broad band structures and an additive 2nd order polynomial is included to account for stray light in the spectrograph. A spectrum correcting for the Ring effect (Grainger and Ring, 1962) has also been included in the fitting routine, as described in Bussemer (1993). The fit is performed in the 490–520 nm wavelength range for the retrieval of O_3 and in the 435–460 nm wavelength range for the retrieval of NO_2. The squared 2σ error of the spectral retrieval represents the measurement error in the retrieval of profiles. Since the residual of the DOAS fit shows only minor structures, systematical errors are not taken into account for the profile retrieval. Possible sources of error are a principle offset on all $\Delta\mathrm{SCD}$s or a drift with time. Both aspects are tested by the use of different reference spectra in consecutive retrievals.

Figure 2 shows $\Delta\mathrm{SCD}$s of NO_2 and O_3 retrieved from the measurements during the LPMA/IASI balloon flight at Teresina on 30 June 2005 and modelled based on the NO_2 and O_3 profile retrievals described in Sect. 2.3. The oscillating pattern of the $\Delta\mathrm{SCD}$s is a consequence of consecutive limb scans. Since the balloon is floating slightly above the maximum of the NO_2 layer in the stratosphere, the first elevation $\mathrm{EA} = 0.5°$ leads to lower NO_2-$\Delta\mathrm{SCD}$s than measurements looking through the profile maximum somewhat lower in the atmosphere. Accordingly as the viewing direction moves closer to the maximum of the NO_2 layer, the $\Delta\mathrm{SCD}$s increase. They reach a maximum for an elevation $\mathrm{EA} = -2.5°$ and then decrease again while the elevation angles continue to decrease. Here the reference spectrum for the spectral analysis of NO_2 is taken at $\mathrm{EA} = 0.5°$. A more quantitative understanding of the observation is obtained

including radiative transfer modelling which is described in the following subsection.

2.3 Profile retrieval

In our case, the measured set of ΔSCDs constitutes the measurement vector y with components $y_i = \Delta$SCD$_i$ ($i = 1, \ldots, N$) (for the nomenclature see Rodgers, 2000). The state to be retrieved consists of elements $x_{j,k}$, representing the absorber concentration of an atmospheric altitude layer j in temporally subsequent instances numbered by k. Note, that the indices i and k implicitly contain the time t_i at which the measurement y_i is taken and the time T_k for which the profile $x_{j,k}$ is inferred. Hence, we need to introduce a kernel $K_{i,j,k}$ (weighting function), which involves both, time and space weighting,

$$K_{i,j,k} = \frac{\partial y_i}{\partial x_{j,k}} \tag{5}$$

with

$$y_i = \sum_j \sum_k K_{i,j,k} \cdot x_{j,k} + \epsilon_y. \tag{6}$$

The kernel is derived using a two step approach. In a first step the geometrical weighting (BoxAMF) is derived from RTM (Radiative Transfer Model) calculations and is represented by the matrix $L_{i,j}$. Accordingly $L_{i,j}$ gives the sensitivity of the measurement y_i at time t_i to the absorber concentration x_{j,k_0} at an arbitrary time t_{k_0}, i.e. neglecting the time difference between retrieval instance T_k and measurement instance t_i,

$$L_{i,j} = \frac{\partial y_i}{\partial x_{j,k_0}} \tag{7}$$

In the second step, the time weighting matrix $C_{i,k}$ is set up to represent the sensitivity of the measurement y_i at time t_i to the absorber concentration $x_{j,k}$ at time T_k. As the time weighting is simply derived by the inverse of the time lag between measurement and state and therefore does not depend on the measurement geometry, it can be separated from geometrical weighting. The matrices $L_{i,j}$ and $C_{j,k}$ then yield the kernel $\widetilde{K}_{i,j,k}$ considering both, geometrical and time weighting

$$\widetilde{K}_{i,j,k} = L_{i,j} C_{i,k}. \tag{8}$$

It should be pointed out that the forward model requires no chemical modelling, in contrast to the methods used so far (Schofield et al., 2004; Hendrick et al., 2004; Butz et al., 2006). This is due to the fact, that at low SZAs the concentration variation along the light path can be neglected for a specific altitude.
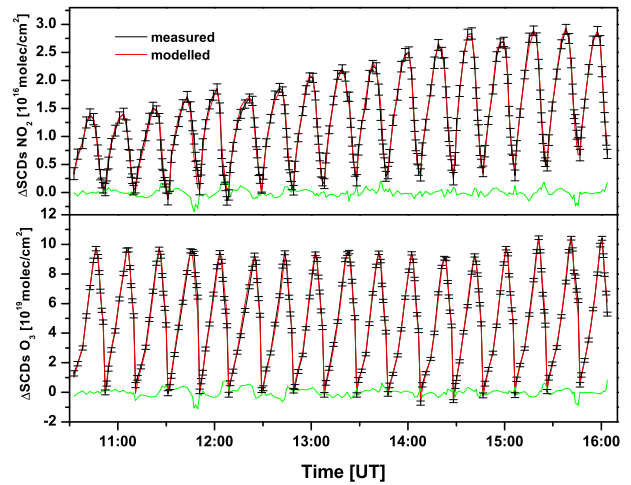

Fig. 2. Measured (black) and forward modeled (red) ΔSCDs for the June 30, 2005 flight. The difference between forward modelled and measured ΔSCDs is shown in green. Upper panel: NO$_2$. Lower panel: O$_3$

a) Radiative transfer modelling

The interpretation of scattered skylight measurements requires radiative transfer modelling. For the individual measurements, the radiative transfer is calculated using the fully spherical radiative transfer model McArtim. McArtim is a backward Monte Carlo model which generates a representative ensemble of individual photon path trajectories through the simulated atmosphere, each defined by a solution of the monochromatic radiative transfer equation at a certain wavelength. The 3 dimensional model was developed at the Institute of Environmental Physics in Heidelberg and validated against other radiative transfer models (Wagner et al., 2007; Deutschmann, 2008). For the present study, a model atmosphere from 0 to 70 km, discretized in layers of 1 km altitude is created, where properties like air density, humidity, aerosol load and temperature are defined. According to the wavelength interval which is considered in the spectral retrieval, the RTM for O$_3$ is modelled at 500 nm and for NO$_2$ at 450 nm.

For ray tracing the light paths from the sun to the telescope, the viewing geometry needs to be defined. Here the balloon height and azimuth angle are obtained from the attitude control systems of the individual payloads. The SZA and SRAA are calculated using this geometrical information. The actual elevation angle of the telescope relative to the payload orientation is controlled by the mini-DOAS instrument itself. As the relative position of the telescope to the gondola affects the absolute EA, it is carefully aligned to the principle axis of the payload prior to the balloon flight. A remaining misalignment can be tested after the flight by comparing the modelled and measured relative radiances for each

observation. The skylight radiance in the UV/vis spectral range changes largely with tangent height near the horizon and shows a wavelength dependent maximum in the lowermost stratosphere (Sioris et al., 2004; Weidner et al., 2005). The stratospheric RT can be properly modelled in volcanically quiet periods, since the variability in the background stratospheric aerosol load barely influences the radiance distribution, and effects of Rayleigh scattering are well known. Tropospheric optical constituents such as aerosols and clouds are only affecting lowest EAs. The resulting viewing geometry is used as input for the RTM.

High frequency pendulum oscillations of the gondola can be accounted for in the RTM calculations by adjusting the effective field-of-view. Since the available records of the attitude control systems indicate a permanent high frequency pendulum oscillation with an amplitude $\Delta EA \geq 0.1°$, the effective field-of-view is expanded to a Gaussian shape with a FWHM of $\sigma = 0.3°$. How remaining and unaccounted pointing errors due to gondola oscillation propagate into the results is discussed in Sect. 2.4.

b) Time weighting

The state $x_{j,k}$ consists of concentration profiles at subsequent times T_k, which are a result of the time grid which is defined prior to the retrieval. Since the retrieval of a single profile requires several measurements y_i, the time grid for the state cannot be the same as for the measurement vector. If the diurnal variation of a certain trace gas is the required state, the time interval between two profiles should still be short enough to reasonably represent the gradient in concentration over time and to allow for the assumption of a linear increase between two instances. For the comparison with measurements performed on different platforms, the time grid should be chosen to match the particular time of the profile to be compared with. For the transformation between the measurement grid and the state grid, a time weighting matrix $C_{i,k}$ is defined, which characterizes the time-lag between the actual measurement and the state. Each measurement y_i at time t_i is assumed to contribute to the two nearest states T_k and T_{k+1} with

$$C_{i,k} = \frac{T_{k+1} - t_i}{T_{k+1} - T_k} \tag{9}$$

$$C_{i,k+1} = \frac{t_i - T_k}{T_{k+1} - T_k} = 1 - C_{i,k} \tag{10}$$

for $T_k \leq t_i \leq T_{k+1}$

and

$$C_{i,k} = 0 \tag{11}$$
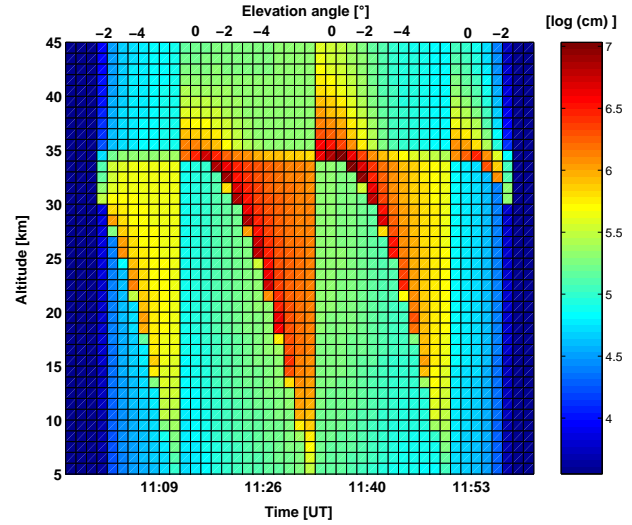
for $t_i < T_k$ and $t_i > T_{k+1}$.

Fig. 3. Logarithm of the kernel $K_{i,j,k}$ for the NO_2 concentration profile at $T_k = 11:30$ UTC. The altitude axis corresponds to the atmospheric layers labeled by j, the time axis corresponds to the measurement instances labelled by i. The example is for limb scans at 35 km altitude with subsequent measurements from EA $= 0.5°$ to EA $= -5.5°$ in steps of $0.5°$.

c) The combined kernel

The combined weighting function matrix $\widetilde{K}_{i,j,k}$, which represents the sensitivity of a measurement to the state is then calculated from the product of $L_{i,j}$ and $C_{i,k}$ (see Eq. 8). However, the differential character of the measurements is not yet taken into account. From Eq. (4) and in analogy to Eq. (6), we find

$$y_i := \Delta SCD_i = SCD_i - SCD_{ref} \tag{12}$$

$$= \sum_j \sum_k \widetilde{K}_{i,j,k} x_{j,k} - \sum_j \sum_k \widetilde{K}_{ref,j,k} x_{j,k} \tag{13}$$

$$= \sum_j \sum_k (\widetilde{K}_{i,j,k} - \widetilde{K}_{ref,j,k}) x_{j,k} \tag{14}$$

and thus, the kernel $K_{i,j,k}$ is defined as

$$K_{i,j,k} = \widetilde{K}_{i,j,k} - \widetilde{K}_{ref,j,k} \tag{15}$$

where the weight of the reference measurement is by definition zero. A consistency proof is the commutability of the reference measurement as it is valid for the spectral approach. Any result of the profile retrieval is invariant to the choice of SCD_{ref}.

As an example, Fig. 3 shows the contributions of the limb scanning measurements at 35 km between $t_i = 10:45$ UTC and $t_i = 12:15$ UTC to the profile at $T_k = 11:30$ UTC. The contribution of the measurements before 11:00 UTC and after 12:00 UTC is zero. Concerning the weighting in altitude, the impact of the varying EA is clearly visible with EA $= -1°$ having the highest sensitivity at float altitude and EA $= -5.5°$

having the highest sensitivity around 15 km. The sensitivity of any measurement y_i to the trace gas column above 40 km is very low, as the light path through the atmosphere above the gondola is nearly equal for all viewing geometries and tends toward the vertical path. As a consequence the difference of $\widetilde{K}_{i,j,k}$ and $\widetilde{K}_{\text{ref},j,k}$, and thus $K_{i,j,k}$ is close to zero for layers j between 40 and 70 km.

For solving the ill-posed problem to retrieve $x_{j,k}$ from Eq. (6), we technically drop index k by queuing $x_{j,k}$ into a 1-dimensional vector x that contains the absorber profiles at consecutive times. In analogy, the kernel $K_{i,j,k}$ is queued into a sparse 2-dimensional matrix $\mathbf{K}$. Equation (6) then reads in matrix notation

$$y = \mathbf{K}x + \epsilon_y. \tag{16}$$

As long as measured optical densities are much smaller than unity, the kernel can be linearly approximated and Eq. (16) can be solved for x in one iteration. In order to obtain a physically reasonable solution from the inversion of Eq. (16) some kind of side-constraint needs to be employed. Null-space and near-null space components (like the concentration of a trace gas above 40 km) of the retrieval are estimated via a priori information (Rodgers, 2000) as it is common practice in this field (Schofield et al., 2004; Hendrick et al., 2004; Weidner et al., 2005). The a priori state x_a is a qualified first guess of x and $\mathbf{S}_a$ is its covariance matrix. A priori profiles used here are inferred from predictions of our photochemical model Labmos (Bösch et al., 2003). The 1-dimensional photochemical model simulates the temporal evolution of certain molecules by executing a set of gas-phase, heterogeneous and photolytic reactions. Initial values are taken from the 3-dimensional chemical transport model SLIMCAT (Chipperfield, 2006). Following Rodgers (2000), the retrieved state $\hat{x}$ is constructed from both, prior information and the measurements, each weighted by the covariances $\mathbf{S}_a$ and $\mathbf{S}_\epsilon$, respectively,

$$\hat{x} = (\mathbf{K}^T \mathbf{S}_\epsilon^{-1} \mathbf{K} + \mathbf{S}_a^{-1})^{-1} (\mathbf{K}^T \mathbf{S}_\epsilon^{-1} y + \mathbf{S}_a^{-1} x_a). \tag{17}$$

The diagonal elements of the measurement covariance $\mathbf{S}_\epsilon$ represent the uncorrelated errors of the ΔSCDs and are the squared DOAS fitting errors. Non diagonal elements represent correlations of ΔSCDs and are set to zero, according to the findings in Sect. 2.2. The optimal estimation method requires an a priori set including a known covariance, e.g. from a climatology, to constrain the inversion. Since the a priori covariance is used here as a tuning parameter, the retrieval is not optimal in its original sense. The entries in the diagonal of the a priori covariance matrix are squared percentages of the a priori value,

$$S_{a_{l,l}} = \frac{p}{100} \cdot x_{a_l}^2 \tag{18}$$

The percentage fraction p is determined by an L-curve method, where the RMS of the deviation of modelled and measured y_i is plotted against the a priori error (e.g. Schofield et al., 2004). p usually ranges between 40 and 80. Additionally, non-diagonal elements are calculated by

$$S_{a_{l,m}} = \sqrt{S_{a_{l,m}} \cdot S_{a_{m,m}} \cdot \exp(-\log_2((l-m)/h)^2)} \tag{19}$$

with h the half width at half maximum (HWHM) of the Gaussian function (or length scale h) (Rodgers, 2000). Sensitivity runs with varying h are performed (e.g. Hendrick et al., 2004) in order to maximize the number of degrees of freedom of the retrieval. For the retrieval of 10 NO_2 profiles (see Fig. 10), a maximum is found for h = 0.5 (see Fig. 4), which corresponds to a correlation length of 1 km. This finding is in agreement with the resolution indicated by the width of the averaging kernels (see Fig. 9). Using non-diagonal elements in the a priori covariance matrix provides a link between different elements of the state vector. In our case it combines information from different altitudes, and hence constrains the smoothness of the profile.

2.4 Characterization of the retrieval and error analysis

The retrieved concentration profiles $\hat{x}$ require thorough characterization of the retrieval with respect to altitude resolution, information content, random errors and systematic errors related to uncertainties of the viewing geometry. A comparison of forward modelled and measured ΔSCDs yields a first check of our method's ability to explain the measurements (see Fig. 2). A quantitative measure for the consistency of measured and forward-modelled ΔSCDs is the root mean square of the difference of both quantities.

$$\text{RMS} = \frac{\sqrt{(\sum_l y_l - y_{l,\text{mod}})^2}}{\overline{y_l}} \tag{20}$$

where $y_{l,\text{mod}}$ is given by the product of $K_{l,m}$ and x_m. The lowest achievable RMS is in the order of the measurement error.

A more sophisticated characterization of the retrieval is performed by calculating the averaging kernel matrix $\mathbf{A}$, which gives the relation between the true value of the state $\mathbf{x}$ and the retrieved state $\hat{\mathbf{x}}$.

$$\hat{\mathbf{x}} = \mathbf{x_a} + \mathbf{A}(\mathbf{x} - \mathbf{x_a}) + \epsilon_x. \tag{21}$$

$\mathbf{A}$ is calculated from the weighting function and covariance matrices by

$$\mathbf{A} = \frac{\partial \hat{\mathbf{x}}}{\partial \mathbf{x}} = (\mathbf{K}^T \mathbf{S}_\epsilon^{-1} \mathbf{K} + \mathbf{S}_a^{-1})^{-1} \mathbf{K}^T \mathbf{S}_\epsilon^{-1} \mathbf{K}. \tag{22}$$

In the ideal case $\mathbf{A}$ is the identity matrix, meaning that the retrieved profile results only from the measurements with an altitude and time resolution as high as the resolution of the chosen grid, thus rendering any additional a priori constraint
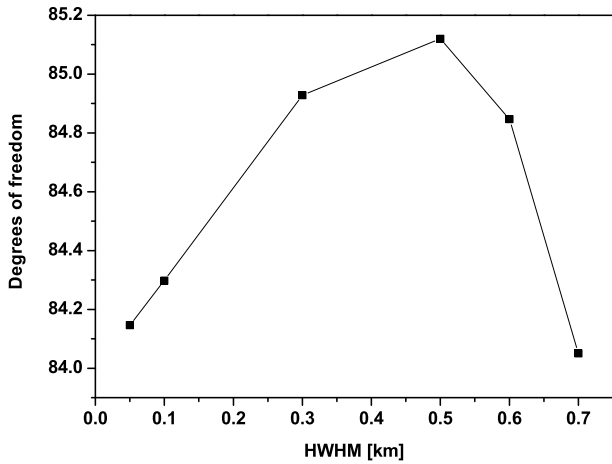
Fig. 4. Number of degrees of freedom of the retrieval (trace of the averaging kernels matrix A) plotted as a function of the half width at half maximum h. This curve applies to the retrieval of NO_2 profiles from limb scanning measurements.

Fig. 5. Two dimensional averaging kernel for the retrieval of NO_2 at 33 km, at 14:00 UTC in June 2005.

dispensable. In practice, the entries in the diagonal of the averaging kernels are often less than unity and extend into neighbouring layers, indicating contributions of the a priori as well as a coarser resolution than the retrieval grid.

A row l of the averaging kernel matrix is referred to as the averaging kernel of the respective state vector element x_l. Remembering that our state vector $\boldsymbol{x}$ is a sequence of concentration profiles in time, we can view the averaging kernels of individual state vector elements x_l as a function of altitude and time (Schofield et al., 2004). Figure 5 illustrates such a time and altitude dependent averaging kernel for the retrieved state vector element at 33 km altitude at 14:00 UTC. The plot indicates that the information for this retrieved value originates from a confined region in space and time. The time and space resolution in this case is 1.5 km and 1 h, respectively. Here, it should be pointed out that the altitude resolution is a result of the measurement geometry while the time resolution is a result of the chosen time grid. Both, altitude and time resolution depend on the sampling frequency. As the time dependent contribution is somehow intuitive, the averaging kernels are typically displayed for a fixed time, in which the altitude resolution becomes more evident. This representation of the averaging kernels is used in Figs. 7 and 9.

The averaging kernel concept offers the possibility to calculate several quantities that characterize the information content of the retrieval. The sum of the diagonal elements of the averaging kernel matrix is a measure of the degrees of freedom in the retrieval. In order to quantify the independence from the a priori, the sum of each individual averaging kernel (one row of $\mathbf{A}$) can be calculated. This is known as the area of an averaging kernel, or – for all averaging kernels – as the measurement response profile. A quantitative measure for the resolution of the profiles is the Backus-Gilbert spread (Backus, 1970), given by
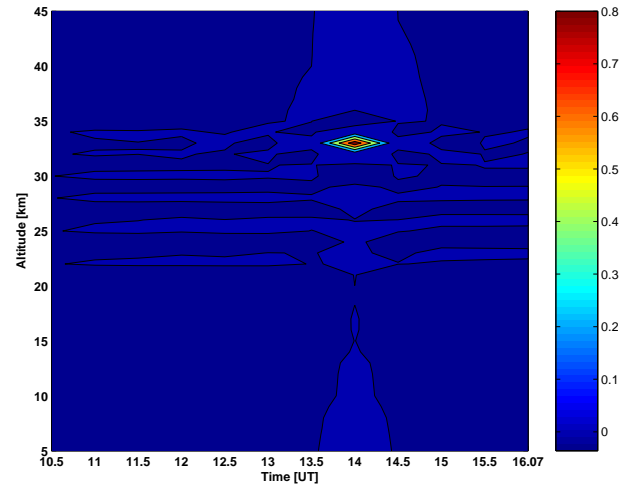
$$s_l = \frac{12 \sum_m (l-m)^2 A_{l,m}^2}{\sum_m A_{l,m}^2}. \tag{23}$$

Besides the averaging kernel matrix, the retrieved state is characterized by errors due to measurement noise, errors due to uncertainties of forward model parameters, and smoothing errors (Rodgers, 2000). For estimating the latter, the a priori covariance $\mathbf{S}_a$ is required to be the covariance of a real ensemble of states (Rodgers, 2000). Here, we use $\mathbf{S}_a$ as a tuning parameter for the regularization strength. Thus, we do not attempt to calculate the smoothing error, but consider the retrieved profile as smoothed by the averaging kernels. The error due to measurement noise is given by the retrieval noise covariance

$$\mathbf{S}_{\text{noise}} = (\mathbf{K}^T \mathbf{S}_\epsilon^{-1} \mathbf{K})^{-1}. \tag{24}$$

Further errors are caused by forward model parameters $\boldsymbol{b}$, which are input parameters that influence the state but are not retrieved. For atmospheric measurements, they typically include atmospheric conditions such as aerosol load, cloud coverage and, most importantly in our case, the viewing geometry. The covariance due to each forward model parameter can be evaluated from

$$\mathbf{S}_f = \mathbf{G_y}^T \mathbf{K}_b^T \mathbf{S}_b \mathbf{K}_b \mathbf{G_y} \tag{25}$$

with

$$\mathbf{G_y} = \frac{d\hat{\mathbf{x}}}{d\mathbf{y}} = (\mathbf{K}^T \mathbf{S}_\epsilon^{-1} \mathbf{K} + \mathbf{S}_a^{-1})^{-1} \mathbf{K}^T \mathbf{S}_\epsilon^{-1}. \tag{26}$$

$\mathbf{G_y}$ is the gain matrix expressing the sensitivity of the retrieved profile to changes in the measured ΔSCDs. $\mathbf{K}_b$ denotes the kernel concerning a particular forward model parameter, $\mathbf{S}_b$ its error covariance. It is found that forward model errors arising from uncertainties in the aerosol loading

are negligible for our limb scanning measurements at 35 km altitude. Also the influence of viewing geometry related errors of SZA and SRAA are found negligible. Forward model errors are dominated by the uncertain knowledge of the elevation angle EA. However, since $\mathbf{K}_{EA}$ is highly non-linear, its numerical calculation would require an iterative approach. Alternatively we estimate the error covariance $\mathbf{S}_{osci}$ due to EA pendulum oscillations of the gondola via a sensitivity study.

EA pendulum oscillations are caused by wind shear acting on the balloon or by insufficient damping of the gondola azimuth stabilization system. Using a record of the attitude control parameters obtained during the MIPAS-B flight in 2005, a sensitivity study is performed, on how the EA oscillations propagate into the retrieved profile. As indicated in Fig. 6, different types of oscillations occurred during the flight. For the sensitivity study, the oscillations around 13:15 UTC (type I) and 14:15 UTC (type II) are treated separately. Type I and type II show frequency regimes of roughly 7×10^{-3} Hz and ≥ 1 Hz with amplitudes of 0.5° and 1.5°, respectively. In order to quantify the error caused by these EA oscillations, the kernel $\mathbf{K}_{osci}$ for an oscillating gondola is simulated using the RTM with oscillating EA data as input. We then calculate a synthetic measurement vector $\boldsymbol{y}_{osci}$ via

$$\boldsymbol{y}_{osci} = \mathbf{K}_{osci} \boldsymbol{x}_a, \tag{27}$$

where $\boldsymbol{x}_a$ acts as the true state vector for our simulation. We then retrieve $\hat{\boldsymbol{x}}_{osci}$ from $\boldsymbol{y}_{osci}$ and the standard kernel $\mathbf{K}$ that is not affected by EA oscillations of the gondola. The difference between input $\boldsymbol{x}_a$ and retrieved $\hat{\boldsymbol{x}}_{osci}$ yields an estimate of the forward model error caused by EA oscillations. As illustrated by Fig. 6, EA oscillations with frequencies lower than the inverse time resolution of the measurements cause oscillations in the retrieved profile, a phenomenon similar to a blurred photograph. EA oscillations with frequencies larger than the inverse time resolution of the measurements lead for EA$\approx$0° to an enhanced contribution of light coming from lower atmospheric layers compared to the forward modelling assumptions. Thus, the retrieved profile maximum is in this case unrealistically shifted downward. This effect depends on the shape of the profile and the viewing geometry and cannot be generalized. The envelope of the squared differences between $\boldsymbol{x}_a$ and $\hat{\boldsymbol{x}}_{osci}$ forms the diagonal of the corresponding covariance matrix $\mathbf{S}_{osci}$. The error in the retrieved profile increases with increasing amplitude of the gondola oscillation and with the spatial distance to the observed object. As the float altitude for the considered balloon flight is around 34 km, both effects are more pronounced in the O_3 retrieval with a maximum at around 26 km than for NO_2 with a maximum at around 32.5 km, thus leading to a higher $\mathbf{S}_{osci}$ for O_3 than for NO_2. For other balloon flights, EA oscillations typically exhibit much smaller amplitudes than used for the present sensitivity study as can be concluded from an inspection of the measured ΔSCDs. Accordingly, the oscillation

errors for the case studies presented in the following section amount to only 50% of the $\mathbf{S}_{osci}$ inferred here.

The total error of the retrieved profile is readily calculated from the sum of the retrieval noise, Eq. (24), and the EA oscillation error $\mathbf{S}_{osci}$,

$$\hat{\mathbf{S}} = (\mathbf{K}^T \mathbf{S}_\epsilon^{-1} \mathbf{K})^{-1} + \mathbf{S}_{osci} \tag{28}$$

3 Results and inter-comparison to results from other methods

We present first O_3 and NO_2 retrievals from limb scanning mini-DOAS measurements based on the method described in Sect. 2. The observations were conducted aboard the MIPAS-B payload on 14 June 2005, and aboard the LPMA/IASI payload on 30 June 2005. Both stratospheric balloon flights were launched at Teresina (5.1° S, 42.8° W) in tropical Brazil. For O_3, we find time independent concentration fields, whereas NO_2 undergoes a significant diurnal variation over the course of our measurements as expected from photochemical considerations. Our O_3 and NO_2 are validated by an in-situ O_3 sonde launched in the vicinity of the balloon flight (Sect. 3.1) and by NO_2 retrievals from space-borne limb observations by the SCIAMACHY instrument (Sect. 3.2).

3.1 Inter-comparison of O_3 profiles from mini-DOAS to an in-situ measured O_3 profile

In order to validate the retrieved O_3 profiles, an ozone profile measured by the mini-DOAS instrument aboard the MIPAS-B payload is compared to an in-situ measured O_3 profile. The sonde data are taken from an electrochemical cell launched at the same station in the vicinity of the balloon flight, the same day at 02:00 UTC. For the comparison a time averaged O_3 profile between 13:00 and 16:00 UTC is derived from our limb measurements. As the ozone concentration is expected to vary little with time in the tropics, the time lag of half a day between the two measurements is negligible. The number of degrees of freedom for a single profile is 5.2. For comparison the higher resolution in-situ measured O_3 profile is degraded to the altitude resolution of the lower resolution mini-DOAS O_3 profile using the averaging kernel matrix $\mathbf{A}$ of the mini-DOAS. The smoothed in-situ sonde profile $\boldsymbol{x}_s$ is derived from the unsmoothed sonde profile $\boldsymbol{x}_h$ through

$$\boldsymbol{x}_s = \boldsymbol{x}_a + \mathbf{A}(\boldsymbol{x}_h - \boldsymbol{x}_a), \tag{29}$$

where $\boldsymbol{x}_a$ is the a priori profile used for the mini-DOAS retrieval (Connor et al., 1994; Hendrick et al., 2004; Butz et al., 2006). Figure 7 shows both ozone profiles and the averaging kernels $\mathbf{A}$ of the mini-DOAS retrieval. The difference between the two profiles is $\leq 12\%$ above 24 km and on average 20% below this altitude and mostly smaller than the errors of the retrieval.
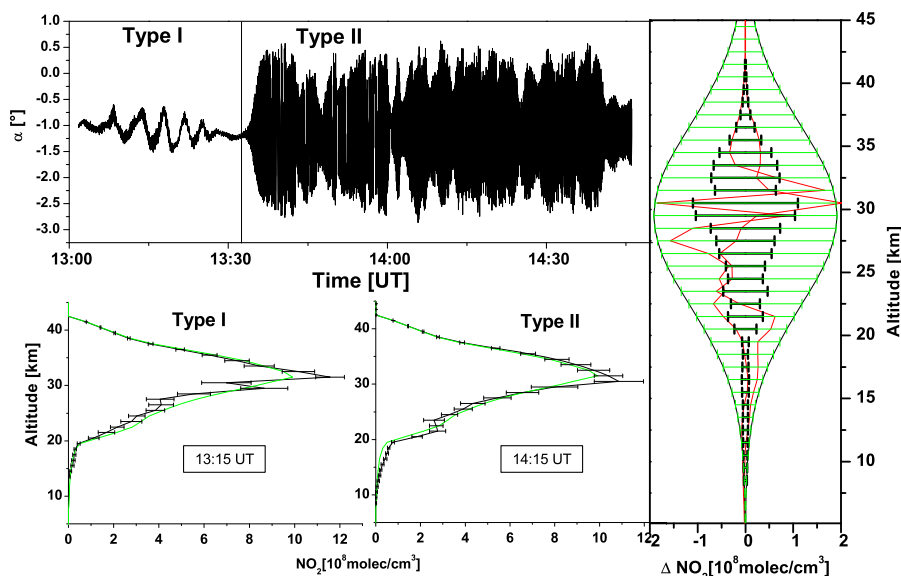
Fig. 6. Upper left panel: extreme case (type I around 13:15 UTC and type II around 14:15 UTC) of pitch angle oscillation of the MIPAS-B gondola, as recorded by the attitude control system. Lower left panel: concentration of NO_2 retrieved from ΔSCDs expected on a calm flight (green) and on a gondola undergoing type I oscillation (black). Lower middle panel: concentration of NO_2 retrieved from ΔSCDs expected on a calm flight (green) and on a gondola undergoing type II oscillation (black). Right panel: differences of retrieved and true profiles for both oscillation types (red), envelope of the differences defined as an upper limit for S_{osci} (green error bars) and noise error S_{noise} (black error bars) for comparison.
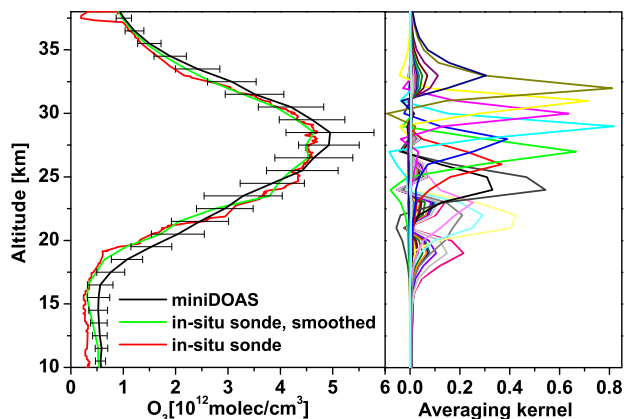

Fig. 7. Left panel: concentration profile of O_3 retrieved from mini-DOAS measurements (black) aboard the MIPAS-B payload on 14 June 2005 and from an in-situ sonde (red) in the vicinity of the balloon flight, smoothed with the averaging kernels of the mini-DOAS retrieval (green). Right panel: Averaging kernels of the mini-DOAS retrieval of O_3. Different colours denote different EA.

Fig. 8. Diurnal variation of NO_2 retrieved from mini-DOAS measurements aboard the LPMA/IASI payload on 30 June 2005. The white arrow marks the time of the SCIAMACHY overpass.

3.2 Inter-comparison of NO$_2$ profiles from mini-DOAS to collocated measurements of the SCIAMACHY instrument

Figure 8 shows the time series of NO_2 profiles retrieved from mini-DOAS observations aboard the LPMA/IASI payload on June 3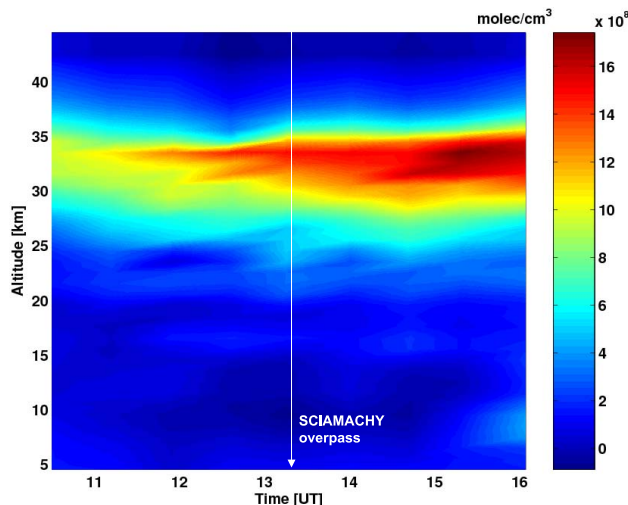0, 2005. The retrieval is performed with a time step (T_k) between different profiles of 30 min. According to expectations based on the stratospheric NO_x/NO_y photochemistry, NO_2 increases during daytime due to its release from N_2O_5 photolysis. The concentration maximum around 33 km altitude increases from about 1×10^9 molec/cm^3 at 10:30 UTC to about 1.6×10^9 molec/cm^3 at 16:00 UTC. As shown exemplarily for the NO_2 profile retrieved at
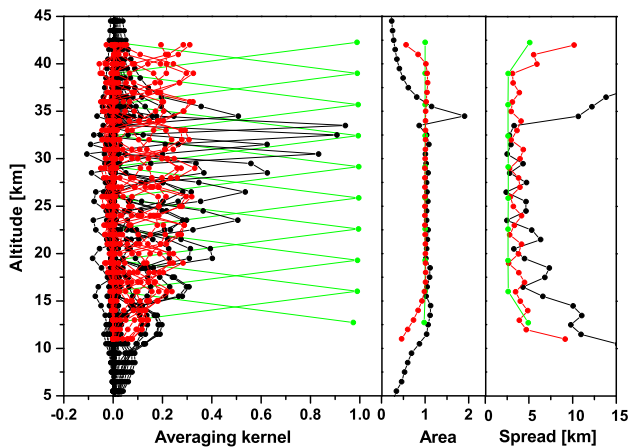
Fig. 9. Characterization of the retrieval of NO_2 as shown in Fig. 10 from balloon-borne measurements from the IUP Heidelberg (black), from SCIAMACHY measurements by the IUP Bremen (red) and MPI Mainz (green). Left panel: averaging kernels. Middle panel: area of the averaging kernels. Right panel: backus-Gilbert spread of the averaging kernels. The degrees of freedom of the retrievals are 10 (IUP Heidelberg), 7.4 (IUP Bremen) and 9.9 (MPI Mainz).

Fig. 10. NO_2 at $SZA = 39°$ on 30 June 2005, retrieved from mini-DOAS measurements aboard the LPMA/IASI payload (5.9° S, 44.5° W) by the IUP Heidelberg (black), and from collocated SCIAMACHY/ENVISAT measurements during orbit 17 427 (2.5° S, 51° W), by the IUP Bremen (red) and by the MPI Mainz (green).

13:15 UTC in Fig. 9, the averaging kernels indicate a high contribution of the measurements to the retrieved profile, as compared to the contributions of the a priori. Also the 2-D averaging kernels in Fig. 5 indicate a reasonable resolution in time and space. Here the total number of degrees of freedom in time and space is 101, which translates into 10 degrees of freedom for a single profile.

We compare our NO_2 retrieval with collocated measurements of the SCIAMACHY instrument (e.g. Burrows et al., 1995; Bovensmann et al., 1999). SCIAMACHY is a UV/visible/near-IR spectrometer (220 nm–2380 nm, FWHM: 0.2 nm–1.5 nm), which was launched aboard the European ENVISAT satellite in March 2002. One of its operation modes is the observation of limb scattered sunlight which allows for the retrieval of NO_2 stratospheric concentration profiles. SCIAMACHY's limb operation mode scans the atmosphere from the ground up to about 90 km altitude in steps of 3.3 km. We compare our NO_2 profile with SCIAMACHY NO_2 retrievals performed by the Max Planck Institute for Chemistry (MPI), Mainz, Germany (Pukite et al., 2006; Kühl et al., 2008), and by the Institute of Environmental Physics (IUP), University of Bremen, Germany (Rozanov et al., 2005).

For comparison with the satellite measurements, our forward model is constructed in a way that the time grid of the retrieved profiles matches the time or actual SZA when the satellite instrument measured a profile at a location closest to our balloon-borne measurements. This criterion is fulfilled for the overpass of SCIAMACHY on 30 June 2005 at $SZA = 39°$ along orbit 17 427. At 13:15 UTC the mini-
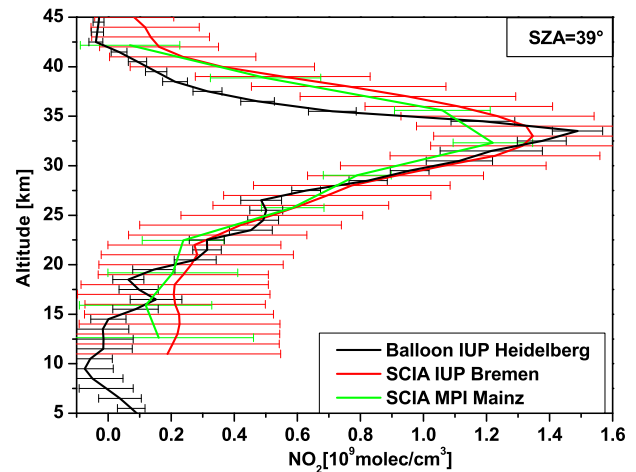
DOAS instrument sampled airmasses at the same SZA, but 570 km to the east of the satellite pixel center. Figure 10 shows the comparison of the mini-DOAS retrieval with the two satellite retrievals. The maximum NO_2 concentration around 34 km of about 1.4×10^9 molec/cm³ compares well for the mini-DOAS IUP Heidelberg and SCIAMACHY IUP Bremen profiles. The SCIAMACHY MPI Mainz profile cannot capture the concentration maximum due to its coarser height grid, but agrees within the error bars. Below the concentration maximum, all three retrievals yield a consistent decrease of the NO_2 concentration with decreasing altitude, with the balloon-borne NO_2 profile including structures, that are not seen or are not as pronounced in the satellite NO_2 profiles. Above the concentration maximum, our mini-DOAS profile decreases rapidly with altitude, while the satellite profiles show a similar decrease but are about 2 km offset towards higher altitudes.

For a quantitative comparison, the retrievals are characterized by common metrics (see Fig. 9), i.e. their averaging kernel matrices, the area and spread of the averaging kernels, and the degrees of freedom, as introduced in Sect. 2.4. Both, the Bremen and the mini-DOAS retrieval are performed on a 1 km grid, while the Mainz retrieval is performed on a coarser height grid of 3.3 km. Specific to the employed retrieval method the averaging kernels for satellite measurements (and therefore their area and spread) are only representative in a range from 11 to 42 km, while for the characterization of the balloon-borne retrieval the range from 0 to 70 km is taken into account. The altitude resolution of the balloon observations, is around 3 km between 15 and 34 km altitude. The area of the averaging kernels of the balloon-borne retrieval is close to unity between 10 km and 35 km. The usage of a

Table 1. Compendium of balloon-borne mini-DOAS measurements

Date Time (UT)	Location	Geophys. Cond. SZA range	Instrument payload	Observation Mode	Retrieval of time dependent profiles
18/19 Aug 2002 15:15–02:38	Kiruna 67.9° N, 21.1° E	high lat. sum. 69.75–94.4° 94.6–88.1°	LPMA/ mini-DOAS	nadir fixed limb	no timedependent profile information
4 Mar 2003 12:55–15:25	Kiruna 67.9° N, 21.1° E	high lat. spring 77.6–88.8°	LPMA/DOAS mini-DOAS	nadir fixed limb	feasible
23 Mar 2003 14:47–17:35	Kiruna 67.9° N, 21.1° E	high lat. spring 78.9–93°	LPMA/DOAS mini-DOAS	nadir fixed limb during ascent scanning limb at float	feasible
9 Oct 2003 15:39–17:09	Aire-sur-l'Adour 43.7° N, 0.25° W	mid-lat fall 66–88°	LPMA/DOAS mini-DOAS	nadir fixed limb	no timedependent profile information
24 Mar 2004 13:55–17:35	Kiruna 67.9° N, 21.1° E	high lat. spring 72–93°	LPMA/DOAS mini-DOAS	fixed limb during ascent scanning limb at float	feasible
14 Jun 2005 09:00–17:10	Teresina 5.1° S, 42.8° W	tropical winter 93–29–33°	MIPAS-B mini-DOAS	scanning limb at float	
17 Jun 2005 18:30–21:30	Teresina 5.1° S, 42.8° W	tropical winter 61–93°	LPMA/DOAS mini-DOAS	fixed limb during ascent scanning limb at float	
30 Jun 2005 09:00–17:00	Teresina 5.1° S, 42.8° W	tropical winter 93–29–33°	LPMA/IASI mini-DOAS	scanning limb at float	
1 Mar 2006 8:00–17:22	Kiruna 67.9° N, 21.1° E	high lat. spring 77–93°	LPMA/IASI mini-DOAS	fixed limb during ascent scanning limb at float	feasible
13 Jun 2008 09:00–13:50	Teresina 5.1° S, 42.8° W	tropical winter 93–29°	LPMA/IASI mini-DOAS	scanning limb at float	EA calibration problem
27 Jun 2008 09:00–21:18	Teresina 5.1° S, 42.8° W	tropical winter 93–29–93°	LPMA/DOAS mini-DOAS	fixed limb during ascent scanning limb at float	EA calibration problem
5 Mar 2009 03:34–05:10	Kiruna 67.9° N, 21.1° E	high lat. spring 77–93°	LPMA/IASI mini-DOAS	scanning limb at float	possible but short timeframe

different number of spectra and constraints leads to a different number of degrees of freedom and a different height resolution for both SCIAMACHY retrievals. The number of degrees of freedom for the satellite retrievals are 7.4 (Bremen) and 9.9 (Mainz), respectively and 10 for the mini-DOAS retrieval.

The comparison of our NO$_2$ vertical profile from a time series of profiles with a measurement which matches in time and space from satellite observations shows good agreement. The difference above 35 km altitude may be due to decreasing sensitivity of the mini-DOAS measurement above balloon float altitude, which is illustrated by a decrease of the area of the averaging kernels. Altogether this provides a positive proof for the applicability of our method to the measurement of time varying radical concentrations. Forthcoming studies will discuss implications of our measurements for stratospheric photochemistry.

4 Conclusion and outlook

The present study proposes a method for the retrieval of time dependent trace gas profiles from balloon-borne UV/vis limb scattered skylight measurements. Retrieval exercises are performed for stratospheric O$_3$ and NO$_2$ exploiting observations of the mini-DOAS instrument aboard the MIPAS-B and the LPMA/IASI balloon payloads in June 2005 over tropical Brazil.

The proposed method involves (a) the spectral retrieval, (b) forward modelling for each measurement, and (c) a suitable inversion algorithm that can handle the spatial and temporal domains. Thereby, our forward model (b) takes into account the relative character of the measurements via a differential weighting function formalism. Balloon-borne mini-DOAS measurements are in that respect self calibrated, i.e. no information on overhead absorbers is necessary. The forward model (b) relies on Monte Carlo radiative transfer modelling of the geometrical light path through the atmosphere

and on a time averaging scheme that considers the temporal distance between the measurements and the state to be retrieved. Therefore, our forward model is well suited for the retrieval of the diurnal variation of UV/vis absorbing radicals. Since the forward model requires no chemical modelling as an input, the retrieval method provides a tool for testing photochemical parameters. Finally, the optimal estimation inverse method (c) provides all tools to thoroughly characterize the retrieved profiles with respect to altitude and time resolution, and error contributions.

Detailed sensitivity studies are performed in order to estimate the systematic error contributions from EA oscillations of the gondola. These sensitivity studies show that, uncorrected EA pendulum oscillations of the gondola potentially lead to considerable errors in the retrieved profiles. Evidently errors due to EA pendulum oscillations increase with the spatial distance between the observer and the object, i.e. for the presented balloon floats at around 34 km altitude the resulting error caused by pendulum oscillations is larger for O_3 then for NO_2. The error arising from these oscillations cannot be generalized, but depends on the strength of the oscillation. Here, 7.5% and 5% are considered for O_3 and NO_2, respectively.

Two comparison studies are performed, where trace gas profiles retrieved from the mini-DOAS measurements are compared to in-situ ozone sonde data and satellite observations of the SCIAMACHY instrument aboard Envisat. The comparisons show good to reasonable agreement confirming the validity of the proposed method. The height resolution of the mini-DOAS measurements is around 3 km between 15 and 34 km altitude. The number of independent parameters in a single retrieved profile depends on the applied time spacing. For example, for the detection of NO_2 the profile retrieval on a half hour time grid for a total of 6 hours observation results in 101 degrees of freedom in 10 profiles, which translates into 10 degrees of freedom for a single profile.

The main advantage of limb scattered skylight measurements from air-borne observation platforms is the ability to monitor the spatial and temporal variation of the targeted radicals during daytime at changing solar illumination. The method is not restricted to sunset or sunrise as is the case for direct sun measurements. Monitoring the diurnal variation of stratospheric radicals may offer new insights into the "reactivity" or oxidation potential of the atmosphere. In particular, new insight might be gained into crucial photochemical parameters important for stratospheric ozone, such as the photolysis frequencies of N_2O_5 and $BrONO_2$ by simultaneous observations of NO_2 and major NO_y species (e.g. the latter by MIPAS-B in the mid-IR), or NO_2, BrO and $BrONO_2$ (e.g. again the latter by MIPAS-B in the mid-IR), respectively, or the efficiency of the ClO/BrO ozone loss cycle by simultaneous observations of the diurnal variation of ClO (e.g., by in-situ resonance fluorescence) and BrO and OClO.

Finally, our study also indicates some drawbacks of the present (intentionally) simplified instrumental set-up. The use of additional sensors providing on-line information on the detector's elevation would largely increase the accuracy of the retrieved vertical profiles. Accordingly, instruments similar in design to the present mini-DOAS instruments but with an on-line viewing angle control have been recently or will be in the near future deployed on aircrafts (Falcon, Geophysica, and HALO) and balloons (MIPAS-B). Moreover, the present retrieval would also benefit from a coupled model of radiative transfer and photochemistry with the result that a retrieval could attempt to directly infer chemical model parameters (such as rate reaction coefficients or photolysis frequencies) from the observations.

Edited by: C. von Savigny

References

Aliwell, S. R., Van Roozendael, M., Johnston, P. V., Richter, A., Wagner, T., Arlander, D. W., Burrows, J. P., Fish, D. J., Jones, R. L., Tornkvist, K. K., Lambert, J.-C., Pfeilsticker, K., and Pundt, I.: Analysis for BrO in zenith-sky spectra: An intercomparison exercise for analysis improvement, J. Geophys. Res., 107, 4199, doi:10.1029/2001JD000329, 2002.

Backus, G.E. and Gilbert, J.: Uniqueness in the inversion of inaccurate gross earth data, Philos. T. Roy. Soc. London A, 266, 123–192, 1970.

Birk, M., Mair, U., Krocka, M., Wagner, G., Yagoubov, P., Hoogeveen, R., Graauw, T., de Stadt, H. van de; Selig, A., Hübers, H.-W., Richter, H., Semenov, A., Koshelets, V., Shitov, S., Ellison, B., Matheson, D., Alderman, B., Harman, M., Kerridge, B., Siddans, R., Reburn, J., Duric, A., Murk, A., Magun, A., Kämpfer, N., and Murtagh, D.: TELIS – development of a new balloon borne THz/submmW heterodyne limb sounder, in: Final Programme, 35th COSPAR Scientific Assembly, Paris, France, 18–25 July 2004, 1690 pp., 2004

Bösch, H., Camy-Peyret, C., Chipperfield, M. P., Fitzenberger, R., Harder, H., Platt, U., and Pfeilsticker, K.: Upper limits of stratospheric IO and OIO inferred from center-to-limb-darkening-corrected balloon-borne solar occultation visible spectra: Impli-

cations for total gaseous iodine and stratospheric ozone, J. Geophys. Res., 108, 4455, doi:10.1029/2002JD003078, 2003.

Bovensmann, H., Burrows, J. P., Buchwitz, M., Frerick, J., Noël, S., Rozanov, V. V., Chance, K. V., and Goede, A. P. H.: SCIAMACHY: Mission Objectives and Measurement Modes, J. Atmos. Sci., 56, 127–150, 1999.

Burrows, J. P., Hölzle, E., Goede, A. P. H., Visser, H., Fricke, W.: SCIAMACHY – Scanning Imaging Absorption Spectrometer for Atmospheric Chartography, Acta Astronaut., 35(7), 445–451, 1995.

Bussemer, M., Der Ring-Effekt: Ursachen und Einfluß auf die spektroskopische Messung stratosphärischer Spurenstoffe, Diploma thesis, Institut für Umweltphysik, Universität Heidelberg, 1993.

Butz, A., Bösch, H., Camy-Peyret, C., Chipperfield, M., Dorf, M., Dufour, G., Grunow, K., Jeseck, P., Kühl, S., Payan, S., Pepin, I., Pukite, J., Rozanov, A., von Savigny, C., Sioris, C., Wagner, T., Weidner, F., and Pfeilsticker, K.: Inter-comparison of stratospheric O3 and NO2 abundances retrieved from balloon borne direct sun observations and Envisat/SCIAMACHY limb measurements, Atmos. Chem. Phys., 6, 1293–1314, doi:10.5194/acp-6-1293-2006, 2006.

Camy-Peyret, C.: Balloon-borne Fourier transform spectroscopy for measurements of atmospheric trace gases, Spectrochim. Acta, 51A, 1143–1152, 1995.

Chipperfield, M. P.: New Version of the TOMCAT/SLIMCAT Off-Line Chemical Transport Model: Intercomparison of Stratospheric Tracer Experiments Q. J. Roy. Meteor. Soc., 132, 1179–1203, doi:10.1256/qj.05.51, 2006.

Connor, B. J., Siskind, D. E., Tsou, J. J., Parrish, A., and Remsberg, E. E.: Ground-based microwave observations of ozone in the upper stratosphere and mesosphere, J. Geophys. Res., 99(D8), 16757–16770, 1994.

Deutschmann, T.: Atmospheric Radiative Transfer Modelling with Monte Carlo Methods, Institute of environmental physics, University of Heidelberg, 82 pp., 2008.

Dorf, M., Butler, J. H., Butz, A., Camy-Peyret, C., Chipperfield, M. P., Kritten, L., Montzka, S. A., Simmes, B., Weidner, F., and K. Pfeilsticker, Long-term observations of stratospheric bromine reveal slow down in growth, Geophys. Res. Lett., 33, L24803, doi:10.1029/2006GL027714, 2006.

McElroy, C. T.: Stratospheric nitrogen dioxide concentrations as determined from limb brightness measurements made on June 17th, 1983, J. Geophys. Res., 93, 7075–7083, 1988.

Fayt, C., and van Roozendael, M., WinDOAS 2.1. Software User Manual, technical report, online available at: http://www.oma.be/BIRA-IASB/Molecules/BrO/WinDOAS-SUM-210b.pdf (last access: July 2010), 2001.

Ferlemann, F., Bauer, N., Fitzenberger, R., Harder, H., Osterkamp, H., Perner, D., Platt, U., Schneider, M., Vradelis, P., and Pfeilsticker, K.: A new DOAS-instrument for stratospheric balloon-borne trace gas studies, Appl. Optics, 39, 2377–2386, 2000.

Grainger, J. F. and Ring, J.: Anomalous Fraunhofer line profiles, Nature, 193, 762–763, 1962.

Harder, J. W., Brault, J.W., Johnston, P., and Mount, G. H.: Temperature dependent NO2 cross-sections at high spectral resolution, J. Geophys. Res., 102, 3861–3879, 1997.

Hendrick, F., Barret, B., Van Roozendael, M., Bösch, H., Butz, A., De Maziere, M., Goutail, F., Hendrick, F., Barret, B., Van Roozendael, M., Boesch, H., Butz, A., De Mazière, M., Goutail,

F., Hermans, C., Lambert, J.-C., Pfeilsticker, K., and Pommereau, J.-P.: Retrieval of nitrogen dioxide stratospheric profiles from ground-based zenith-sky UV-visible observations: validation of the technique through correlative comparisons, Atmos. Chem. Phys., 4, 2091–2106, doi:10.5194/acp-4-2091-2004, 2004.

Hermans, C.: O4 absorption cross-sections, available at: http://spectrolab.aeronomie.be/o2_o4info.htm, (last access: 29 January 2010), 2002.

Kühl, S., Pukite, J., Deutschmann, T., Platt, U., and Wagner, T.: SCIAMACHY limb measurements of NO2, BrO and OClO. Retrieval of vertical profiles: Algorithm, first results, sensitivity and comparison studies, Adv. Space Res., 42(10), 1747–1764, 2008.

Oelhaf, H., von Clarmann, T., Fergg, F., Fischer, H., Friedl-Vallon, F., Fritzsche, C., Piesch, C., Rabus, D., Seefeldner, M., and Völker, W.: Remote sensing of trace gases with a balloon borne version of the Michelson interferometer for passiv atmospheric sounding (MIPAS), in Proc. 10th ESA Symp. on European Rocket and Balloon Programmes and Related Research, ESA-SP-317, 207–213, 1991.

Pfeilsticker, K., Erle, F., and Platt, U.: Observation of the stratospheric NO2 latitudinal distribution in the northern winter hemisphere, J. Atmos. Chem., 32, 101–120, 1999.

Platt, U. and Stutz, J.: Differential Optical Absorption Spectroscopy (DOAS), Principle and Applications, Springer Verlag, Heidelberg, 2008.

Pommereau J. P. and Goutail, F.: O3 and NO2 ground-based measurements by visible spectrometry during arctic winter and spring 1988, Geophys. Res. Lett., 15, 891–894, 1988.

Pukite, J., Khl, S., Deutschmann, T., Wilms-Grabe, W., Friedeburg, C., Platt, U., and Wagner, T.: Retrieval of stratospheric trace gases from SCIAMACHY limb spectra, Proceedings of the first Atmospheric Science Conference, Frascati, Italy, 8–12 May, 2006.

Rodgers, C. D.: Inverse methods for atmospheric sounding, World Scientific, Singapore, New Jersey, London, Hongkong, 2000.

Rothman, L. S., Jacquemart, D., Barbe, A., Chris Benner, D., Birk, M., Brown, L. R., Carleer, M. R., Chackerian, C., Chance, K., Dana, V., Devi, V. M., Flaud, J.-M., Gamache, R. R., Goldman, A., Hartmann, J.-M., Jucks, K. W., Maki, A. G., Mandin, J.-Y., Massie, S. T., Orphal, J., Perrin, A., Rinsland, C. P., Smith, M. A. H., Tennyson, J., Tolchenov, R. N., Toth, R. A., Vander Auwera, J., Varanasi, P., and Wagner, G.: The HITRAN 2004 Molecular Spectroscopic Database, J. Quant. Sectrosc. Ra., 96, 139–204, 2005.

Rozanov, A., Bovensmann, H., Bracher, A., Hrechanyy, S., Rozanov, V., Sinnhuber, M., Stroh, F., and Burrows, J. P.: NO2 and BrO vertical profile retrieval from SCIAMACHY limb measurements: Sensitivity studies, Adv. Space Res., 36(5), 846–854, doi:10.1016/j.asr.2005.03.013, 2005.

Schofield, R., Connor, B. J., Kreher, K., Johnston, P. V., Rodgers, C. D.: The retrieval of profile and chemical information from ground-based UV-visible spectroscopic measurements, J. Quant. Sectrosc. Ra., 86, 115–131, 2004.

Sioris C. E., Kurosu, T. P., Martin, R. V., and Chance, K.: Stratospheric and tropospheric NO2 observed by SCIAMACHY: first results, Adv. Space Res., 34, 780–785, 2004.

Toon, G. C.: The JPL MkIV interferometer, Opt. Photonics News, 2, 19–21, 1991

Voigt, S., Orphal, J., Bogumil, K., and Burrows, J. P.: The Temperature dependence (203-293K) of the absorption cross-sections of O_3 in the 230-850 nm region measured by Fourier-transform spectroscopy, J. Photochem. Photobiol. A, 143, 1–9, 2001.

Wagner, T., Burrows, J. P., Deutschmann, T., Dix, B., von Friedeburg, C., Frieß, U., Hendrick, F., Heue, K.-P., Irie, H., Iwabuchi, H., Kanaya, Y., Keller, J., McLinden, C. A., Oetjen, H., Palazzi, E., Petritoli, A., Platt, U., Postylyakov, O., Pukite, J., Richter, A., van Roozendael, M., Rozanov, A., Rozanov, V., Sinreich, R., Sanghavi, S., and Wittrock, F.: Comparison of box-air-mass-factors and radiances for Multiple-Axis Differential Optical Absorption Spectroscopy (MAX-DOAS) geometries calculated from different UV/visible radiative transfer models, Atmos. Chem. Phys., 7, 1809–1833, doi:10.5194/acp-7-1809-2007, 2007.

Weidner, F., Bösch, H., Bovensmann, H., Burrows, J. P., Butz, A., Camy-Peyret, C., Dorf, M., Gerilowski, K., Gurlit, W., Platt, U., von Friedeburg, C., Wagner, T., and Pfeilsticker, K.: Balloon-borne limb profiling of UV/vis skylight radiances, O_3, NO_2, and BrO: technical set-up and validation of the method, Atmos. Chem. Phys., 5, 1409–1422, doi:10.5194/acp-5-1409-2005, 2005.